MEDICAL ROBOTS

In vivo tissue regeneration with robotic implants

Dana D. Damian,[1,2]* Karl Price,[1]* Slava Arabagi,[3] Ignacio Berra,[4] Zurab Machaidze,[1] Sunil Manjila,[5] Shogo Shimada,[6] Assunta Fabozzo,[7] Gustavo Arnal,[1] David Van Story,[1] Jeffrey D. Goldsmith,[1] Agoston T. Agoston,[8] Chunwoo Kim,[9] Russell W. Jennings,[1] Peter D. Ngo,[1] Michael Manfredi,[1] Pierre E. Dupont[1]†

Robots that reside inside the body to restore or enhance biological function have long been a staple of science fiction. Creating such robotic implants poses challenges both in signaling between the implant and the biological host, as well as in implant design. To investigate these challenges, we created a robotic implant to perform in vivo tissue regeneration via mechanostimulation. The robot is designed to induce lengthening of tubular organs, such as the esophagus and intestines, by computer-controlled application of traction forces. Esophageal testing in swine demonstrates that the applied forces can induce cell proliferation and lengthening of the organ without a reduction in diameter, while the animal is awake, mobile, and able to eat normally. Such robots can serve as research tools for studying mechanotransduction-based signaling and can also be used clinically for conditions such as long-gap esophageal atresia and short bowel syndrome.

INTRODUCTION

Robotics has been successfully applied to the restoration of human health and to the augmentation of human capabilities. Clinically approved robots are available for performing minimally invasive surgical procedures (1, 2) and for assisting stroke victims in relearning motor control tasks (3, 4). Robotic prostheses have been designed to replace human limbs (5, 6), and soft and hard exoskeletons are being developed to enhance human strength and endurance (7, 8). However, these types of robots respond only to conscious motion commands. In addition, these robots either remain outside the human body or enter the body for a short period of time, typically the duration of a medical procedure. In contrast, robotic implants represent an unexplored frontier. Such devices can be implanted in the body for an extended period of time and interact mechanically with tissues to regulate tissue forces or fluid flow rates (9) in response to sensed physiological signals and external commands.

One intriguing application for robotic implants is mechanostimulation-modulated tissue regeneration. Whereas in vivo tissue engineering is based on the implantation of a cell-seeded scaffold, an alternate approach is to use mechanical stimulation of existing tissues to induce their growth. Mechanotransduction or cell signaling using mechanical forces is well known to be related to cell proliferation and growth (10–14) and is clinically applied in distraction osteogenesis for inducing bone growth (15), for tissue expanders for producing skin grafts (16), and in wound healing (17). When healthy tissue of the desired type is present in the body, mechanically induced growth can avoid many of the challenges of traditional tissue engineering, for example, cell death before vascularization of the scaffold, immunogenic response to synthetic scaffolds, and mismatch between desired and actual tissue properties (18–20).

The lengthening of tubular organs—such as the esophagus, intestines, and vasculature—is well suited to mechanically stimulated growth

(21–23), although the multifunctional nature of these organs (e.g., providing peristalsis and nutrient absorption) complicates the process in comparison to bone or skin. In addition, the approach in which growth-inducing forces are applied should not compromise organ functionality by occluding flow (22) and, furthermore, should be minimally disabling to the patient, for example, not requiring medically induced sedation and paralysis, as used during treatments of esophageal atresia (21).

We report a robotic implant for tubular organ lengthening that addresses these challenges. It enables both automatic and operator-controlled mechanical force modulation based on sensor measurements of tissue displacement and force. The system serves both as a research tool for studying tissue-scale mechanostimulation and as a precursor to a clinical device. We demonstrate the potential of robotically induced tissue growth through in vivo porcine esophageal lengthening experiments during which the animals were awake, able to eat, and move normally.

RESULTS

We designed the robotic implant, first conceptualized in (24), to attach to the exterior of either disconnected or connected tubular organ segments (Fig. 1, A and B) by two attachment rings. The implant body is positioned adjacent to the organ and is sized to avoid damage to surrounding tissue. It is covered in a smooth biocompatible waterproof skin that completely seals the interior motor, sensors, and electronics from bodily fluids and enables gas sterilization (Fig. 1, C and D). Traction is generated by translation of the lower attachment ring, which can move freely along the implant body due to the folds in the skin.

The open-ring geometry of the attachment rings (Fig. 1E) maintains the diameter of the lengthened organ while enabling attachment to both disconnected (Fig. 1A, esophageal atresia) and connected (Fig. 1B, bowel and vasculature) organ segments. Because the rings and implant are exterior to the organ, they do not occlude internal flow. The rings attach to the implant by sliding connectors, allowing them to be first sutured to the organ without the implant obstructing the surgical field (Fig. 1F). To avoid the potential of creating a leak if a suture was to tear out of the tissue, we placed the sutures so that they do not penetrate the organ lumen.

[1]Boston Children's Hospital, Harvard Medical School, Boston, MA 02115, USA. [2]University of Sheffield, Sheffield S13JD, UK. [3]Helbling Precision Engineering, Cambridge, MA 02142, USA. [4]National Pediatric Hospital J.P. Garrahan, Buenos Aires 01712, Argentina. [5]McLaren Bay Neurosurgery Associates, Bay City, MI 48706, USA. [6]University of Tokyo Hospital, Tokyo 1138655, Japan. [7]Hospital of Padua, Padua 35128, Italy. [8]Brigham and Women's Hospital, Harvard Medical School, Boston, MA 02115, USA. [9]Korea Institute of Science and Technology, Seoul 02792, Republic of Korea.
*These authors contributed equally to this work.
†Corresponding author. Email: pierre.dupont@childrens.harvard.edu
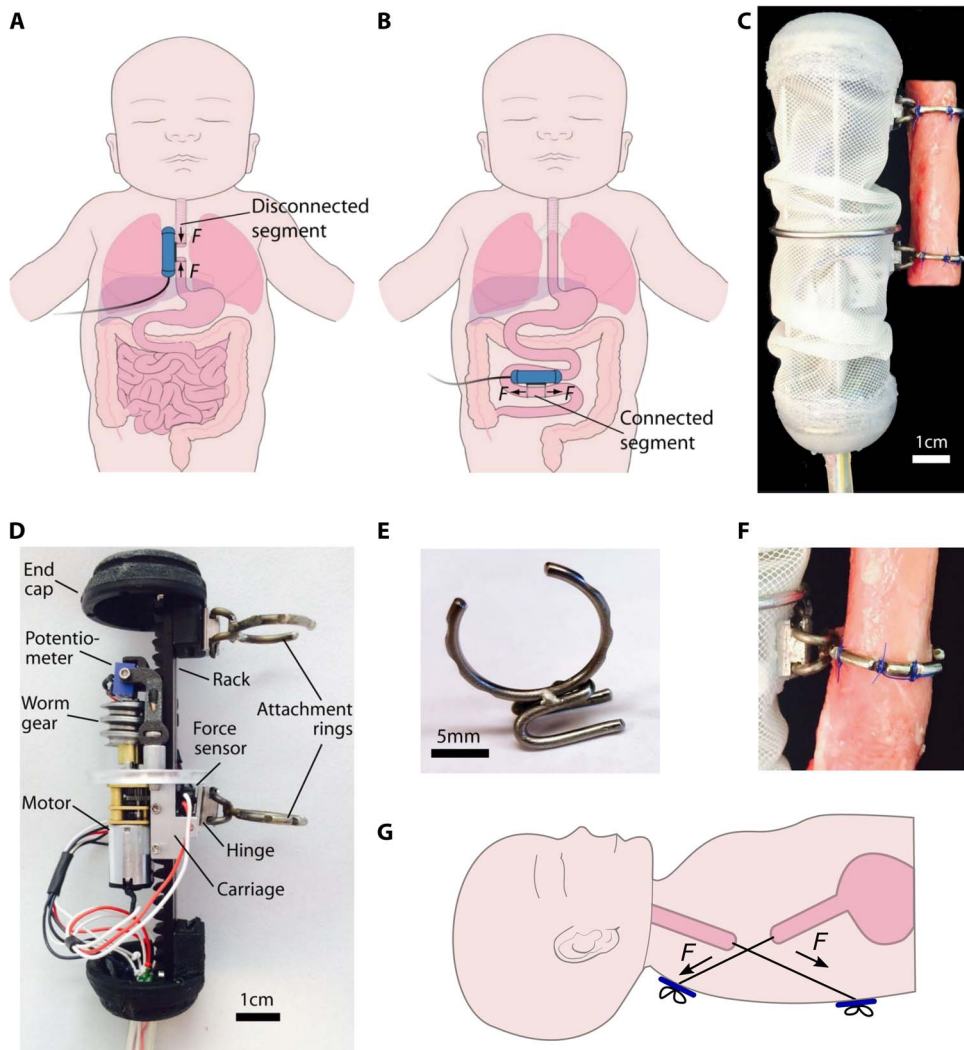
Fig. 1. Robotic implant for tubular tissue growth. (**A**) For the treatment of long-gap esophageal atresia, the implant applies forces (*F*) to disconnected esophageal segments. After inducing sufficient growth, the segments are surgically connected to form a complete esophagus. (**B**) As a potential treatment for short bowel syndrome, the implant applies forces (*F*) to connected segment of bowel. By inducing sufficient lengthening to support the absorption of necessary calories and fluids, a dependence on intravenous feeding could be reduced or eliminated. (**C**) The robot is covered by biocompatible waterproof skin and is attached to tubular organ by two rings (esophageal segment shown). The upper ring is fixed to the robot body, whereas lower ring translates along the body. (**D**) Robot with skin removed to show motor drive system and sensors. Rotation of worm gear causes the lower ring to translate along the body. (**E**) Rings detach from robot body to facilitate attachment to tubular organ. (**F**) Tissue is attached to the ring using sutures. (**G**) In the Foker technique for treating long-gap esophageal atresia (*21*), sutures externalized on the patient's back are used to apply forces (*F*) to esophageal segments.
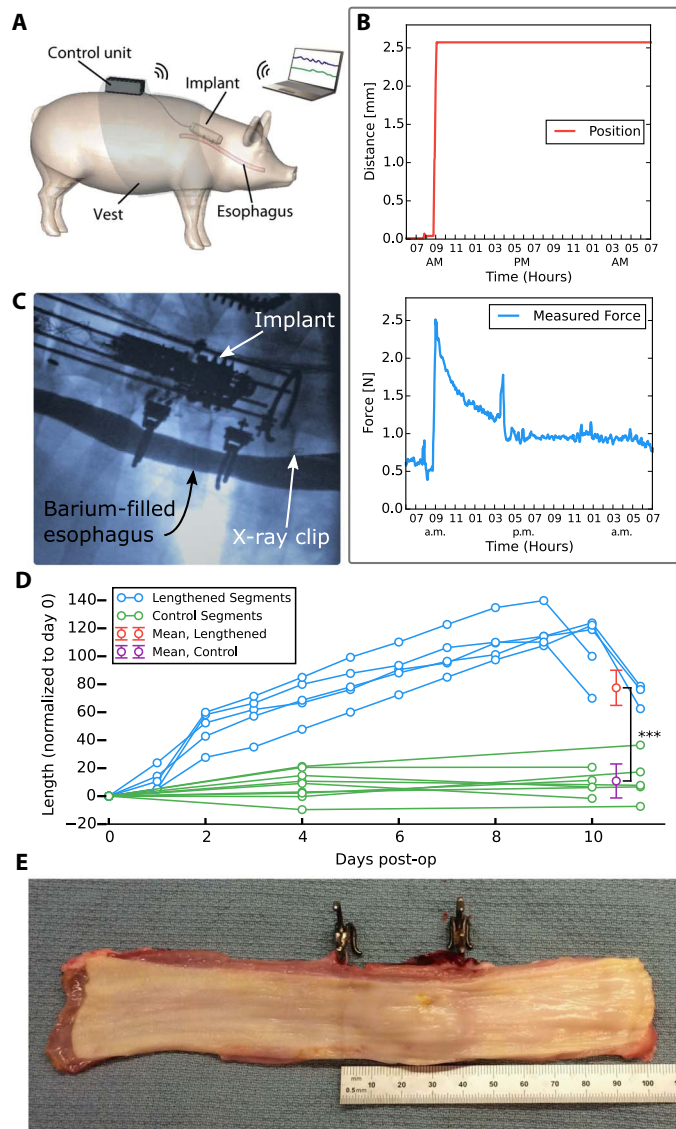
The implant was designed such that the only forces it generates are equal, opposite, and collinear forces applied to the tubular organ (Fig. 1, A and B). This strategy decouples traction forces from the patient's physiological movement to avoid the risks and lifestyle impairment associated with some current techniques. For example, in the clinical treatment of long-gap esophageal atresia, forces applied to the esophageal segments are generated via passive reaction forces on the patient's back (Fig. 1G) (*21*). Patients are maintained in a state of sedation and paralysis in the intensive care unit (ICU) for the duration of traction (1 to 4 weeks) so that the sutures do not tear out of the esophagus due to musculoskeletal motion.

The implant body contains a motor that controls the position of the lower ring and sensors that measure the distance between the rings and the force on the lower ring (Fig. 1D). The implant's microcontroller, communication chip, and battery power supply are located in a wearable control unit outside the host, which is connected by cable to the implant body (Figs. 2A and 3D). The microcontroller was programmed to provide a variety of functionality. For the studies reported here, a basic control mode was used in which the force applied by the rings or the distance between them could be commanded wirelessly from a laptop computer that is also used for data logging and visualization (Fig. 2A). This mode was used for two reasons. First, we wanted to mimic the daily fixed displacements of clinical practice. Second, for reasons of animal safety in testing a new device, we wanted to be present to ensure that the animal was not undergoing distress when traction was adjusted. More complex robotic control is also possible, such as removing the applied force when the implant detects that the animal is feeding.

We experimentally verified the capability of the robotic implant to induce tubular tissue growth on healthy connected esophagus in swine. This approach combines the more stringent implant size requirement of esophageal lengthening (Fig. 1A) with evaluation of the organ's transport ability during traction, as is necessary during bowel lengthening (Fig. 1B). Two groups of animals were used: a surgical group (*n* = 5) that received the implant and a naïve group (*n* = 3) that did not. In the surgical group, the rings were sutured to the esophagus at an initial separation distance of 20.2 ± 0.8 mm. To track esophageal lengthening outside the traction zone (e.g., due to animal growth), we marked control segments 20 mm proximal and 20 mm distal to the attachment rings using pairs of x-ray–visible surgical clips. Each pair of clips marked an ~20-mm segment. In this way, each animal acted as its own control so that tissue changes due to the presence of the implant could be distinguished from changes due to applied force.
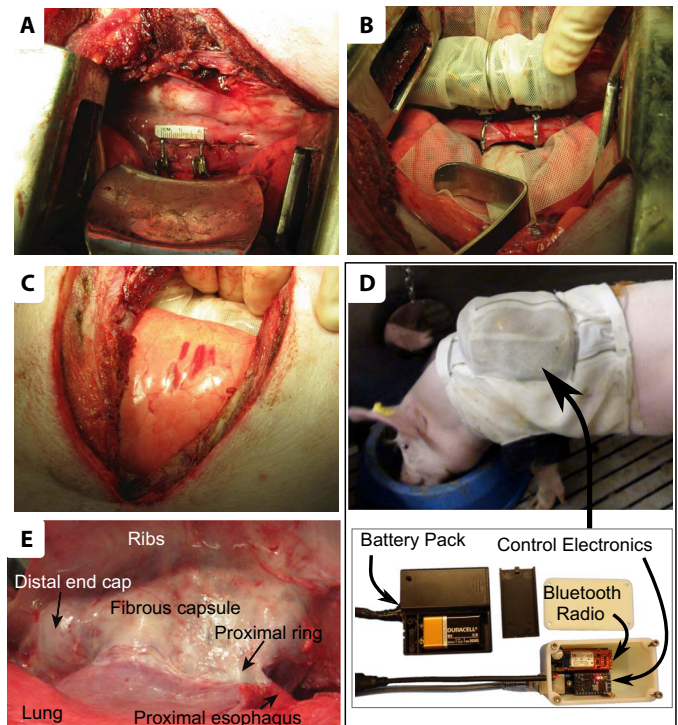
Traction was started 2 days after implantation (day 2), and ring separation distance was increased by an average of 2.5 mm each day (Fig. 2B) through day 9 (*n* = 2) or day 10 (*n* = 3). After a rapid increase in ring separation distance, the measured force was observed to increase equally rapidly and then decrease with an approximately exponential decay over the subsequent 24-hour period (Fig. 2B). However, the daily ring displacement ensured that the force and strain on the

Fig. 2. Esophageal lengthening experiments. (**A**) An implant controller located in a vest pocket communicates wirelessly with a laptop computer. (**B**) Force and position data recorded over a 24-hour period. (**C**) Fluoroscopic image showing the flow of contrast agent through esophagus during traction. (**D**) Esophageal segment length versus time. Surgery occurs on day 0. Segment length corresponds to the distance between implant attachment rings for lengthened segment (blue) and that between clips for control segments (green). Average values at sacrifice are given (in red and purple, respectively). Two animals were survived to day 10, and three were survived to day 11. ***$P < 0.0001$. (**E**) Resected esophagus cut along its length and unrolled along its circumference to show epithelium. Rings are placed adjacent to attachment locations for reference. Note the normal appearance of tissue and the uniform diameter of the lengthened section.

Fig. 3. Implant surgery. (**A**) Suturing of rings to the esophagus. (**B**) A silicone sheet is inserted behind the esophagus, and the implant is connected to attachment rings. (**C**) Implant and esophagus, wrapped in silicone sheet, positioned between the rib cage and right lung before surgical closure. (**D**) Control electronics are housed in a vest pocket. (**E**) Necropsy view of a fibrotic capsule surrounding the implant. Bulges due to proximal ring and distal end cap can be seen in capsule.

expressed normal appetite, consumed the provided amount of food (based on animal weight and age), and passed stool. Despite having undergone a major surgery, all animals gained weight (weight gain of 2.2 ± 1.3 kg). The implant-reported distance between the rings was in agreement with the distance, as derived from x-ray and fluoroscopic images taken to assess the adjustments on days 0 and 4 and on the final day (day 10 or 11) (Fig. 2D).

On the final day, to measure total elongation in vivo, we iteratively adjusted the ring separation distance to remove the residual force and strain and then recorded the corresponding ring distance. The distances before and after removal of residual strain are shown in Fig. 2D. The zero-strain length increased by 77 ± 13% (mean ± SD), over the 8 to 9 days of force application. These measurements, which were in agreement with physical measurements taken at necropsy (Fig. 2E), demonstrated a statistically significant increase with respect to the clip-marked esophageal sections above and below the implant, which increased in length by 10 ± 12%.

In congruity with clinical practice, a fibrous capsule (Fig. 3E) formed around the silastic sheet (Fig. 3C) enveloping the implant and esophagus. The capsule was found to be easily removable from both the implant and the esophagus.

Although esophageal lengthening is performed clinically, there is controversy as to whether the esophageal segments are growing or simply stretching (25). To investigate this, we first studied the geometry of the lengthened samples. The excised esophagi were cut longitudinally and unrolled, showing a healthy appearance of the mucosa (Fig. 2E). The tissue width (esophagus circumference) measured 8.2 ± 1.4 mm

loaded segment did not reach zero, owing to the lengthening that occurs over the subsequent 24-hour period. Note that the force spikes in Fig. 2B occurring at 7:30 a.m. and 4:00 p.m. correspond to meal times when the pig was eating.

The animals did not display any signs of discomfort due to adjustment, and fluoroscopic examination indicated normal flow through the stretched region (Fig. 2C and movie S1). Furthermore, all animals

between the rings and 8.9 ± 1.5 and 8.7 ± 2.1 mm in the proximal and distal control segments, respectively, indicating that the tissue was uniform along the entire length and that elongation preserved lumen diameter within a fraction of a millimeter.

The cross section of the esophagus is composed of five tissue layers (Fig. 4A): the muscularis externa, submucosa, muscularis mucosa, lamina propria, and epithelium (26). The muscularis externa is the thickest layer and is composed of a mixture of skeletal and smooth muscle cells arranged in longitudinal and circular sublayers. The structure of this layer facilitates investigation into whether lengthening is due to growing or stretching, as described below.

To measure how the thickness of this layer may have changed, we studied tissue samples stained with Masson's trichrome. Statistical analysis shows that the thickness of the lengthened muscular layer was preserved with respect to the adjacent control segments and also with respect to tissue taken from the naïve group (Fig. 5A).

Because both the circumference and thickness of the muscularis externa are maintained during lengthening, its volume has increased. Further testing was performed to understand whether this volume in-

crease was due to cellular hypertrophy, proliferation, the generation of fibrosis, or a combination of these effects.

To explore whether lengthening could be attributed to muscle cell hypertrophy, we compared skeletal muscle fiber cross section in both circular and longitudinal muscle layers of the muscularis externa (Fig. 4B). We found no statistically significant difference in fiber cross section between the lengthened tissue and tissue collected from the set of naïve swine, indicating that lengthening is not due to muscle hypertrophy (Fig. 5B).

We also used 4′,6-diamidino-2-phenylindole (DAPI) immunofluorescent staining to compare the nuclear density of the muscularis externa in the surgical group with naïve swine tissue (Fig. 4C) and found no statistically significant difference (Fig. 5C). The observed trend of increasing nuclear density from proximal to distal segments can be explained as follows. The muscular layers in the esophagus are a mixture of skeletal and smooth muscle cells. The ratio of skeletal to smooth cells varies along its length, with a larger proportion of skeletal muscle cells in the proximal region and a smaller proportion in the distal region. Smooth muscle has a larger number of nuclei than skeletal muscle, and so, the observed variation in nuclear density is to be expected.

We also quantified the nuclear density of the inner epithelial layer, which does not vary in composition along the esophageal length. No statistical difference in nuclear density was found between the three regions of the surgical and naïve groups (Fig. 5D).
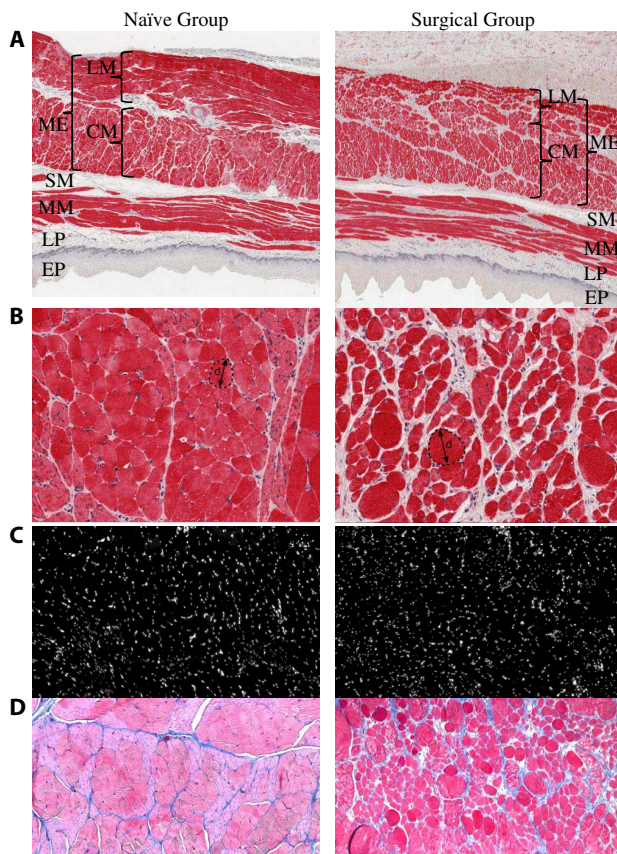
As a definitive demonstration of cellular proliferation, we compared nuclear proliferation in the muscle cells of the muscularis externa using a Ki-67 and Desmin staining protocol. We observed a statistically significant increase in proliferation of muscle cells in the lengthened tissue compared to tissue from the naïve group (Fig. 5E).

All of these results indicate that tissue growth has occurred. To quantify in the muscle layers what fraction of lengthening is due to muscle cell proliferation and what fraction is due to fibrosis, we used Masson's trichrome staining to quantify the relative fraction of muscle and collagen measured by area (Fig. 4D). In the naïve animal tissue, the muscle/collagen ratio was 93%:7%. In the lengthened segments, the muscle/collagen ratio was 80%:20% (Fig. 5F). As detailed in Materials and Methods, because the collagen is interspersed between groups of muscle cells, these ratios can be used to divide the average lengthening of 77% into components due to muscle cell proliferation (49%) and collagen proliferation (28%). Put another way, 63% of lengthening is due to muscle cell proliferation, and 37% is due to collagen formation (compared to 93%:7% if the original ratio of muscle/collagen had been maintained).

Fig. 4. Esophageal tissue histology. (**A**) Longitudinal sections of Desmin-stained tissue (×1 magnification) showing tissue layers: muscularis externa (ME), which is composed of longitudinal muscle (LM) and circular muscle (CM); submucosa (SM); muscularis mucosa (MM); lamina propria (LP); and epithelium (EP). (**B**) Longitudinal sections of Desmin-stained tissue (×20 magnification) illustrating diameter measurement of skeletal muscle fiber cross sections. (**C**) Longitudinal sections of DAPI-stained tissue (×10 magnification) used to assess nuclear density. (**D**) Longitudinal sections of Masson's trichrome–stained tissue (×20 magnification) for measuring relative fractions of muscle (pink) and collagen (blue).
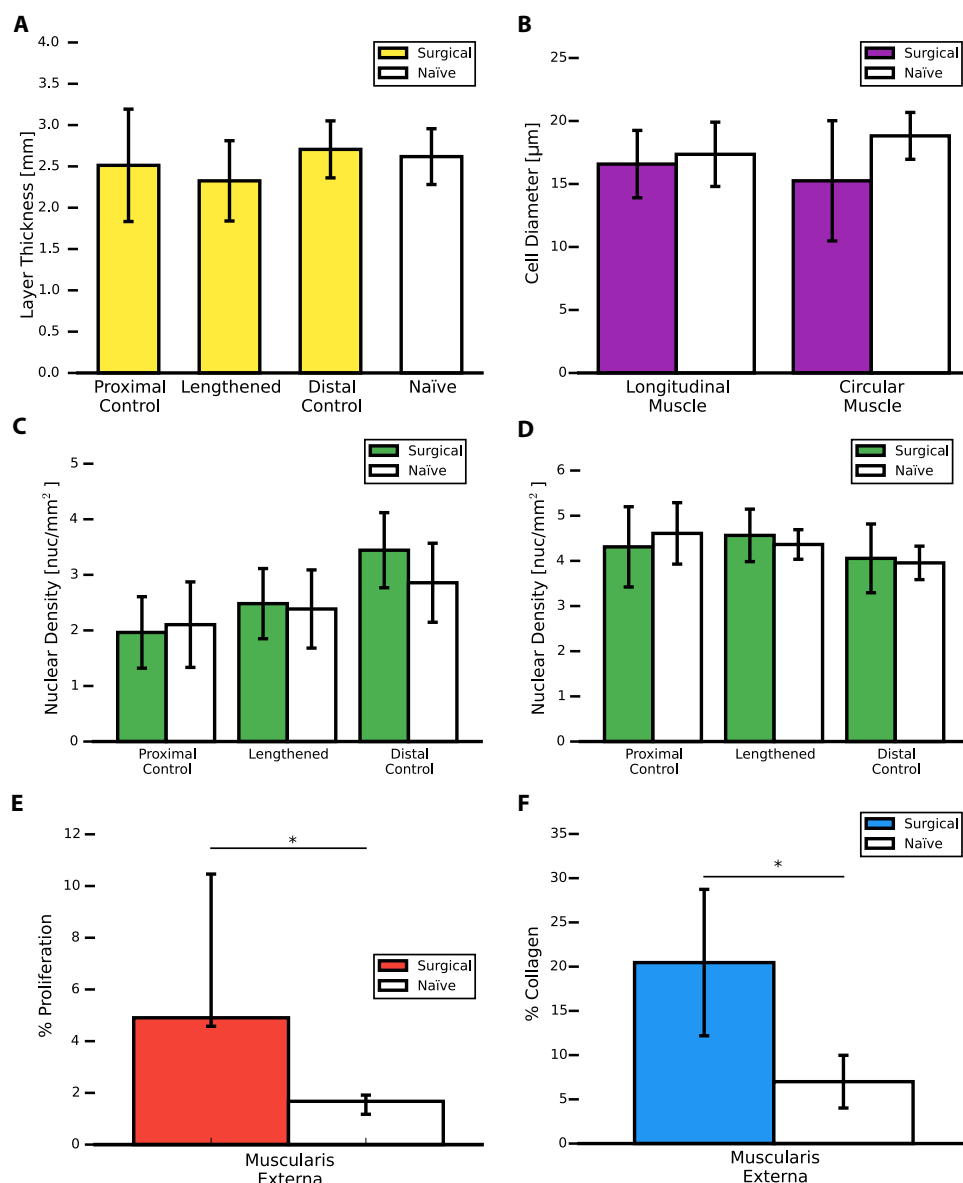
DISCUSSION

These results demonstrate in a large animal model that esophageal traction–induced lengthening is not due to stretching (change in cross-section dimensions or cellular hypertrophy) but rather a combination of cellular proliferation and fibrosis. Our robotic implant establishes that lengthening of tubular organs can be achieved in a precisely controlled manner that maintains organ geometry, preserves organ functionality, and eliminates the need for patient immobilization during growth. Furthermore, by exploiting tissue-level mechanostimulation, the standard challenges of tissue engineering are avoided.

Robotic implants offer substantial benefits compared to the static approaches currently applied to esophageal, bone, and skin growth. This includes the capability to apply dynamic time-varying strains

Fig. 5. Histology results comparing surgical and naïve groups. Asterisks indicate *P* < 0.05 with specific values given in subcaptions. Error bars indicate 1 SD, unless otherwise noted. (**A**) Thickness of muscularis externa. (**B**) Skeletal muscle fiber diameter in longitudinal and circular layers of muscularis externa comparing lengthened surgical and naïve segments. (**C**) Nuclear density of muscularis externa. (**D**) Nuclear density in epithelium. (**E**) Median percentage proliferating muscle cells in muscularis externa of lengthened surgical segment versus naïve tissue. Error bars represent first and third quartiles (*P* = 0.025). (**F**) Percentage of collagen in lengthened surgical segment versus naïve tissue (*P* = 0.002).

provides the capability to study these mechanisms and to apply what is learned clinically to optimize organ morphology, function, and growth rate.

Robotics also provides the ability to respond autonomously to changes in the biological system. A simple example is adapting the adjustment of strain to accommodate actual growth during the lengthening process. Some existing methods adjust tissue loading by the same amount every day, resulting in a daily decrease in applied strain as the tissue lengthens. In other cases (e.g., skin expansion), the amount of adjustment is based on palpation to assess tissue tightness and perfusion. A force- or pressure-sensing robotic device can be programmed to consistently provide the desired level of strain by regularly recalibrating itself to account for actual growth.

More complex interaction with the biological host is also possible, such as removing the applied strain when the implant senses specific physiological activity. For example, in our porcine experiments, it was possible to detect when the animal was eating on the basis of force spikes (Fig. 2B). Although our monitoring of the animals indicated that the applied strain did not cause them discomfort while swallowing, the robotic implant could have removed the applied force until it sensed that the animal had finished eating. Similarly, in bowel lengthening, a robotic implant could be programmed to detect peristalsis and relax for a period of time to facilitate passage of food.

Although robotics can significantly enhance mechanostimulated organ growth, there are potential limitations to what it can achieve. For example, long-gap esophageal atresia, as a congenital condition, is treated when patients are children and growing. Bone lengthening and skin expansion are performed successfully in adults, but it is unknown whether the mechanisms that induce lengthening in the pediatric esophagus are still active in adults. Furthermore, the nerves controlling esophageal contraction run along its length. In cases of esophageal atresia, the nerves are interrupted and do not fully regenerate after anastomosis. Despite impaired peristalsis, the repaired esophagus, aided by gravity in humans, successfully performs its main function as a conduit to the stomach. In our swine studies, the continued effectiveness of the esophagus was demonstrated by normal function of the alimentary canal and by animal weight gain. Even if esophageal motility were to have some impairment from growth induction, the ability to achieve an intact esophageal conduit would remain preferable to surgical alternatives, such as esophageal replacement, where normal esophageal motility would not be expected.

based on the physiological processes of the tissue. In clinical practice, strain adjustments for esophageal, bone, and tissue expansion are performed in discrete steps on a daily or weekly basis. Such clinical regimens, as reproduced in the experiments reported here, do induce organ growth but can also alter tissue properties (e.g., produce fibrosis). However, it is well known that tissue responds not only to static strains but also to dynamic loading. Examples from tissue engineering include skeletal muscle (*27*), smooth muscle (*28*), cartilage (*29*), and arteries (*30*). Furthermore, periodic relaxation of traction may enhance tissue perfusion. In addition, although mechanotransduction has been studied on the cellular level (*10, 11*), little is known at the organ level about the mechanisms governing mechanostimulated organ growth. Robotics

Beyond their use for organ growth, robotic implants represent a new direction in medical robotics. These bionic systems can assist in performing normal body functions either temporarily, until the body repairs itself, or permanently. The ongoing miniaturization of sensors (31) and actuators (32), together with the continuing development of techniques for wireless communication, power transfer (33, 34), and energy scavenging (35), may lead to devices surpassing even those proposed in science fiction.

MATERIALS AND METHODS
Robot design
The structural components of the robot are fabricated from stiff waterproof polymers (Fig. 1D). These consist of the rack (machined Delrin, reinforced with a $^1/_{16}''$-diameter stainless steel rod) and two end caps molded from urethane resin (Smooth-Cast ONYX Slow, Reynolds Advanced Materials). Three additional stainless steel rods ($^1/_{16}''$ diameter) attached to the two caps act as an endoskeleton to stiffen the frame and also to prevent surrounding tissue from herniating into the mechanism.

The robotic mechanism comprised a machined aluminum carriage that slides along the rack under the control of a motor-driven (298:1 gear box, 40-oz·in torque, Pololu Corp.) worm gear (A1C55-N24, SDP/SI). The worm gear is nonbackdriveable, meaning that when the motor is turned off, the position of the carriage does not change. A potentiometer (652-3266W-1-103LF, Bourns Inc.) rotating with the worm gear measures the displacement of the carriage along the rack and is fixed to a steel frame (polished gray steel; Shapeways) that attaches to the carriage. The lower ring is attached to the carriage by a hinge joint that transmits the tensile force applied by the tissue on the ring to a force sensor (FSS Low Profile Force Sensors, FSS1500NST, Honeywell Inc.) mounted on the carriage.

The tubular organ is attached to the implant by two rings (Fig. 1, C to F). Six sutures spaced equally about the circumference are used to attach each ring to the esophagus. The design is intended to provide uniform distribution of traction forces around the organ's circumference to support tubular growth and to minimize the chance of the sutures tearing out of the tissue. The rings are fabricated from welded $^1/_{16}''$-diameter stainless steel rod stock. The open-ring design enables attachment to connected organs and adjustment of ring diameter (Fig. 1E). Grooves on the outer surface of the ring prevent suture from sliding along or off the ring. To enable the rings to be first sutured to the organ and then attached to the implant, each ring includes a U-shaped connector. This connector slides onto a mating T-shaped stainless steel connector located on the outside of implant's encapsulation (Fig. 1, E and F).

Robot encapsulation
The robot mechanism and electronics are completely sealed inside a biocompatible medical-grade encapsulation that permits sterilization using ethylene oxide. The main encapsulation component is a 0.070″-thick cylindrical silastic skin (PR72034-007R, Bentec Medical) that is reinforced with an embedded polyester mesh. Rather than being stretched taut between the end caps, excess material is used to create folds on each side of the moving attachment ring (Fig. 1C). This allows the ring to translate along the implant body without stretching the silastic skin, which would interfere with ring force measurement and also increase the required motor torque. Molded silastic caps (MDX4-4210, Dow Corning Corp.) seal each end of the cylindrical skin. Elec-

trical conductors are encased in a 20-French silastic tube (GS75160-20, Bentec Medical) integrated with the bottom cap and attached to Ethernet connectors. The I-shaped connectors for the tissue attachment rings are clamped to the underlying mechanism by screws that pass through the encapsulation. These attachments and all joints of the encapsulation were sealed using a medical-grade silicone adhesive (Type A, Dow Corning Corp.). The weight of the encapsulated implant is 99.4 g, and the rings weigh 3.5 g.

Control and communication
The implant is connected by cable to a wearable control unit located outside the body that integrates all circuitry related to control, sensing, and communication with a battery power supply (Figs. 2A and 3D). The main electronic components are a microcontroller (Baby Orangutan B-328, Pololu Corp.), a differential amplifier (MCP6001, Microchip Technology Inc.) for the force sensor, a voltage regulator, and a Bluetooth transmitter module (BlueSMIRF Silver, Sparkfun Electronics). The power supply consisted of four 9-V batteries connected in parallel. A low-level controller (programmed in C++) uses Proportional Integral Derivative control to position the moving attachment ring to achieve control commands consisting of either a desired ring-to-ring spacing or a desired ring force. Control commands are received via Bluetooth from a laptop computer. These commands can be entered individually or can be preprogrammed to produce a desired waveform, for example, adjustment once per day or every few minutes. Sensor data are streamed to the laptop by Bluetooth at a sampling frequency of 6.6 Hz. A graphical user interface on the laptop allows real-time data plotting, control command entry, controller gain adjustment, and emergency stopping of the motor.

Animal groups
Two animal groups were used in these experiments. Both groups comprised young Yorkshire female pigs of about the same weight (43.5 ± 3.7 kg, mean mass ± 1 SD) and age (14.4 ± 1.0 weeks). The surgical group ($n = 5$) underwent esophageal lengthening, as described below. Within this group, three animals underwent 9 days of lengthening, and two animals underwent 8 days of lengthening. The difference in duration was due solely to procedure scheduling constraints. The naïve control group ($n = 3$) underwent no surgical procedure. For both groups, tissue samples were collected immediately after animal sacrifice.

Surgical procedure and animal care
The surgical procedure was inspired by the Foker technique for the clinical treatment of long-gap esophageal atresia (Fig. 1G) (21). In this technique, suture loops are attached to the ends of the esophagus and passed through intercostal spaces to be tied off against force-distributing buttons positioned on the baby's back. Suture force is manually increased each day by inserting short lengths of millimeter-diameter tubing between the suture loops and buttons. During the 1 to 4 weeks of traction, patients are maintained in a state of sedation and paralysis in the ICU so that the sutures do not tear out of the esophagus due to musculoskeletal motion.

Animal care followed procedures prescribed by the Institutional Animal Care and Use Committee. After induction of anesthesia, the animal was intubated and placed on ventilation. A right thoracotomy was performed at the seventh intercostal space, and the esophagus was dissected from the surrounding adventitia. A tunnel was created at the ninth intercostal space, and the implant cable was passed through it and connected to the control box. Keeping the implant body within

the sterile field, but outside the surgical cavity, the two attachment rings were sutured to the esophagus at a nominal separation distance of 20 mm (Fig. 3A). In addition, two pairs of titanium clips (LIGACLIP Extra Ligating Clips, LT300, Ethicon LLC) were placed 20 mm proximal and distal to the rings. The clips in each pair were placed 20 mm apart to provide the means to track lengthening of the esophagus outside the traction region. These segments are referred to as the proximal control segment and the distal control segment.

Subsequently, the robot was placed in the right thorax and attached to the rings (Fig. 3A). To prevent adhesions of the esophagus to surrounding tissue and to protect the lungs, we wrapped a silastic sheet (PR72034-007R, Bentec Medical) around the dissected esophagus and implant (Fig. 3B). The sheet was sutured to itself, forming a cylinder, and also sutured to the esophagus to prevent it from sliding along the organ (Fig. 3C). The right thorax was closed in three layers. Two chest tubes were used to remove air from the pleural cavity.

Patency of the esophagus and operability of the implant were assessed immediately after surgery using x-ray or fluoroscopy. The pig was then dressed in a vest (SAI Infusion Technologies) containing a zippered pocket on its back into which the control unit and batteries were placed. The animal was then weaned from anesthesia. During the subsequent days of the experiment, the animals were fed two times per day with a slurry diet consisting of milled grains, water, and juices. They also received omeprazole (to limit stomach acid), cephalexin (antibiotic), and fentanyl (pain reliever). The batteries were changed once per day. The animals gained 2.2 ± 1.3 kg in weight between surgery and sacrifice. In addition to immediately after surgery, imaging was also performed on day 4 and on the final day (10 or 11).

Daily implant adjustment
After allowing the animals to recover for one full day, we initiated traction on the morning of day 2. During this first traction adjustment, the rings were advanced sufficiently to apply a force of ~2 N to the segment between the rings. This corresponded to an average displacement of 7.2 ± 2.4 mm. Subsequent adjustments were performed each morning at about the same time (9:00 a.m.), with the distance between the rings increased by an average of 2.5 mm per day (Fig. 2, B and D).

Segment length measurement
The implant provided continuous length measurement of the segment undergoing traction. X-ray and fluoroscopic images taken on days 0 and 4 and the final day (day 10 or 11) were used to measure the length of the proximal and distal control segments. Before sacrifice, the implant was adjusted in an iterative fashion to remove the traction force from the lengthened segment. This was performed over a 10- to 15-min period to allow for tissue relaxation. The ring distance corresponding to zero force was taken as the final segment length. These measurements were in good agreement with manual measurements of the excised tissue. The lengths of the control segments and stretched segment are plotted in Fig. 2D. The data for the proximal control segment in one animal were discarded because the measurement indicated that at least one of the clips had become detached from the esophagus.

Physical measurement of lumen diameter
To measure the lumen diameter, we cut the wall of the excised esophagus longitudinally and unrolled it to a rectangular shape (Fig. 2E). Width measurements of the esophagus in this configuration represent the circumference of the lumen.

An image of each esophagus was taken with a ruler next to it. Using ImageJ (National Institutes of Health), 20 width measurements were made for each of the three segments of interest (proximal control, lengthened, and distal control) in the surgical group. Sixty measurements of width were taken for each esophagus in the naïve group. Average lumen circumferences were computed from these data sets.

Histology
Esophageal tissue samples were collected from each animal in the surgical and naïve groups. Both longitudinal and transverse samples were prepared by fixing in 10% neutral-buffered formalin and then embedded in paraffin. Sections were cut and stained with Masson's trichrome using routine histological protocols. DAPI fluorescent staining was used for characterizing nuclear density. To quantify muscle cell proliferation, we developed a double stain protocol for porcine esophagus using an anti-Desmin protein antibody (1:4000 dilution; D8281, Sigma-Aldrich) and a Ki-67 antibody (1:250 dilution; VP-RM04, Vector Laboratories). Sequential double staining was performed on the Leica Bond III staining platform. Antigen retrieval was performed using Bond Epitope Retrieval 1 for 30 min. Ki-67 was detected and developed using the Bond Polymer Refine Detection kit, and Desmin was detected and developed using the Bond Polymer Refine Red Detection kit. Specimens were visualized using a microscope (BX53, Olympus America Inc.), and image acquisition was carried out using the AxioVision Microscopy Software (version 4.8.2, Carl Zeiss Microscopy) and ImageScope (version 12.3.0.5056, Leica Biosystems GmbH).

Thickness of the muscularis externa
To measure layer thickness, we used longitudinally cut Masson's trichrome–stained samples. Three images at ×5 magnification, evenly spaced along the length of the tissue, were taken. The filenames were blinded using an MD5 hash before being measured. Twenty evenly spaced measurements were taken using ImageJ in each of the three images, resulting in 60 measurements per slide for each layer. These measurements were then averaged. A t test was used to compare surgical and naïve control groups. The results are presented in Fig. 5A.

Muscle fiber diameter
To investigate cell hypertrophy, we performed a study of skeletal muscle fiber cross-sectional diameter. Skeletal muscle fibers are visible on Desmin-stained slides and are arranged in both longitudinal and circular layers in the muscularis externa. Fiber diameters were compared because they are less sensitive to sample cutting angle than fiber length. Four longitudinally cut tissue samples were used for the circular muscle layer, and four circumferentially cut tissue samples were used to measure the longitudinal muscle layer. Using ImageJ, the two maximally distant points of each fiber cross section were selected manually, and the software computed the distance between them (Fig. 4B). An average of 120 muscle cell diameters was counted per pig (minimum, 75; maximum, 175). The averages are shown in Fig. 5B. A t test was used to compare surgical and naïve control groups. There was no significant difference in skeletal fiber diameter for either the circular muscle layer or the longitudinal muscle layer.

Nuclear density
Longitudinally cut tissue samples stained with DAPI immunofluorescent stain were used to quantify nuclear density. Up to 12 ×10 magnification images were used when possible, depending on the

amount of available tissue. If the full area of the layer was covered in less than 12 fields of view, then only as many images as were required to cover the entire area of the layer were used. The minimum number of fields used in any one animal was six, and the minimum number of nuclei counted was 1484.

A morphological algorithm was written in Python and OpenCV to count the number of nuclei in each image. Nuclei had a variety of shapes and sizes, and some nuclei appeared in clusters of 20 or more. The algorithm was designed to compensate for these challenges. First, all DAPI-positive contours in the image were identified. Contours were then sorted to eliminate those falling outside minimum and maximum size constraints (based on manual identification of the largest and smallest nuclei in the full data set). The mean nucleus size and SD were then computed from the reduced contour list. All contours were then divided into one of two categories: (i) single nucleus if the area of the contour is less than the median or larger than the median but higher than 84% circularity and (ii) multinucleus cluster if the area is larger than the median area, smaller than the median area plus 2 SDs and low circularity, or larger than the median area plus 2 SDs. The number of nuclei in a multinucleus cluster was estimated according to the following equation: $\# \text{nuclei} = \text{round}\left(\frac{\text{Cluster area}}{\text{Mean nucleus area}}\right)$. This algorithm gave good agreement with manual counting on sample images.

The nuclear density of both the lengthened and naïve samples was observed to increase along the length of the esophagus. This corresponds to the increasing ratio of smooth to skeletal muscle cells along the length of the esophagus. Smooth muscle cell clusters have a much higher nuclear density than skeletal muscle cells, leading to higher densities at distal locations. On the basis of a t test, comparisons of the densities of the lengthened and naïve tissue segments in each of the three sections show that they are not statistically different.

Nuclear proliferation at time of sacrifice

To provide a direct measurement of cell proliferation at the time of sacrifice, we used a dual Ki-67 and Desmin staining protocol to both detect proliferating nuclei and associate nuclei with muscle cells. We computed the percentage of Ki-67–marked muscle cell nuclei in the muscularis externa in the surgical and naïve groups.

Longitudinal tissue samples were used to quantify nuclear proliferation. Eight images at ×32 magnification were used. Total nuclei were counted from the digital photographs of these fields. The names of the files were blinded before counting. Ki-67–marked nuclei were counted blind through the eyepiece of the microscope because a high fidelity of color was required to distinguish proliferating cells from nonproliferating cells. The percentage of proliferating muscle nuclei was shown to be larger in the surgical group compared to the naïve group (Fig. 5E), as computed with the Mann-Whitney U test.

Percentage of lengthening due to muscle versus collagen (fibrosis)

The muscularis externa is composed of groups of smooth and skeletal muscle cells interconnected by collagen, as shown in Fig. 4D. Given this structure, tissue along the direction of lengthening is composed partially of muscle and partly of collagen. To compute how much of the lengthening was due to muscle cell proliferation and how much was due to collagen proliferation, we considered lines parallel to the direction of elongation and measured the ratio of the lengths of the cell types intersecting these lines. Computing the average ratio over all possible lines in a tissue region is equivalent to computing the ratio of cell-type areas in that region.

We used longitudinal Masson's trichrome–stained tissue samples from the lengthened segments in the surgical group and from the naïve group. Eight ×10 magnification images of the muscularis externa were obtained if sufficient tissue was available on a slide. If the full area of the layer was covered in less than eight fields of view, then only as many images as were required to cover the entire area of the layer were used (minimum fields used was three).

For each animal, a set of three color thresholds in the Hue Saturation Value representation were chosen. Red represented muscle, blue represented collagen, and white represented a void of tissue in the image. Once the thresholds were set, an algorithm written in Python and OpenCV was used to threshold each image into three parts, removed the tissue voids, and tallied the area of each tissue type.

Using this method, the muscle/collagen ratio of naïve tissue was found to be 93%:7%. In lengthened tissue, the muscle/collagen ratio was 80%:20% (Fig. 5F). Because the ratio changed, we need to solve a set of linear equations to determine the fraction of lengthening due to muscle cell proliferation versus the fraction due to collagen proliferation. By defining the variables [L^i=, total initial tissue segment length; δ=, increase in tissue segment length; $l_m^i = 0.93 L^i$=, initial length composed of muscle cells (measured in naïve tissue); $l_c^i = 0.07 L^i$=, initial length composed of collagen (measured in naïve tissue); $l_m^f = 0.8 (L^i + \delta)$=, final length composed of muscle cells; $l_c^f = 0.2(L^i + \delta)$=, final length composed of collagen], we can solve for the lengthening due to muscle and collagen proliferation using the following equations:

$$\frac{(l_m^f - l_m^i)}{L^i} = \frac{(0.8\ (L^i + \delta) - 0.93 L^i)}{L^i} = 0.8(0.77) - 0.13 = 0.49$$

$$\frac{(l_c^f - l_c^i)}{L^i} = \frac{(0.2\ (L^i + \delta) - 0.07 L^i)}{L^i} = 0.2(0.77) + 0.13 = 0.28$$

These numbers indicate the segment lengthening due to muscle proliferation alone (49%) and collagen proliferation alone (28%), with their sum yielding the total observed lengthening of 77%. We can also express these numbers as fractions of the total 77% lengthening,

$$\frac{\left(\frac{(l_m^f - l_m^i)}{L^i}\right)}{\left(\frac{\delta}{L^i}\right)} = \frac{0.49}{0.77} = 0.63$$

$$\frac{\left(\frac{(l_c^f - l_c^i)}{L^i}\right)}{\left(\frac{\delta}{L^i}\right)} = \frac{0.28}{0.77} = 0.37$$

These numbers indicate that 63% of lengthening was due to muscle cell proliferation and 37% was due to collagen proliferation.

SUPPLEMENTARY MATERIALS
robotics.sciencemag.org/cgi/content/full/3/14/eaaq0018/DC1
Movie S1. Fluoroscopic video shows in vivo adjustment of implant consisting of an increase in segment length of 2 mm.

REFERENCES AND NOTES
1. N. P. Wiklund, Technology insight: Surgical robots—Expensive toys or the future of urologic surgery? Nat. Clin. Pract. Urol. 1, 97–102 (2004).

2. K. P. Sajadi, H. B. Goldman, Robotic pelvic organ prolapse surgery. *Nat. Rev. Urol.* **12**, 216–224 (2015).

3. G. B. Prang, M. J. A. Jannink, C. G. M. Groothuis-Oudshoorn, H. J. Hermens, M. J. IJzerman, Systematic review of the effect of robot-aided therapy on recovery of the hemiparetic arm after stroke. *J. Rehabil. Res. Dev.* **43**, 171–184 (2006).

4. C. L. Massie, Y. Du, S. S. Conroy, H. I. Krebs, G. F. Wittenberg, C. T. Bever, J. Whitall, A clinically relevant method of analyzing continuous change in robotic upper extremity chronic stroke rehabilitation. *Neuorehabil. Neural Repair.* **30**, 703–712 (2016).

5. M. Goldfarb, B. E. Lawson, A. H. Shultz, Realizing the promise of robotic leg prostheses. *Sci. Transl. Med.* **5**, 210ps15 (2013).

6. L. Resnik, S. L. Klinger, K. Etter, The DEKA Arm: Its features, functionality, and evolution during the Veterans Affairs Study to optimize the DEKA Arm. *Prosthet. Orthot. Int.* **38**, 492–504 (2014).

7. W. Cornwall, In pursuit of the perfect power suit. *Science* **350**, 270–273 (2015).

8. L. N. Awad, J. Bae, K. O'Donnell, S. M. M. De Rossi, K. Hendron, L. H. Sloot, P. Kudzia, S. Allen, K. G. Holt, T. D. Ellis, C. J. Walsh, A soft robotic exosuit improves walking in patients after stroke. *Sci. Transl. Med.* **9**, eaai9084 (2017).

9. E. T. Roche, M. A. Horvath, I. Wamala, A. Alazmani, S.-E. Song, W. Whyte, Z. Machaidze, C. J. Payne, J. C. Weaver, G. Fishbein, J. Kuebler, N. V. Vasilyev, D. J. Mooney, F. A. Pigula, C. J. Walsh, Soft robotic sleeve supports heart function. *Sci. Transl. Med.* **9**, eaaf3925 (2017).

10. J. Folkman, A. Moscona, Role of cell shape in growth control. *Nature* **273**, 345–349 (1978).

11. C. S. Chen, M. Mrksich, S. Huang, G. M. Whitesides, D. E. Ingber, Geometric control of cell life and death. *Science* **276**, 1425–1428 (1997).

12. C. A. Cezar, E. T. Roche, H. H. Vandenburgh, G. N. Duda, C. J. Walsh, D. J. Mooney, Biologic-free mechanically induced muscle regeneration. *Proc. Natl. Acad. Sci. U.S.A.* **113**, 1534–1539 (2016).

13. C.-P. Heisenberg, Y. Bellaïche, Forces in tissue morphogenesis and patterning. *Cell* **153**, 948–962 (2013).

14. C. Huang, J. Holfeld, W. Schaden, D. Orgill, R. Ogawa, Mechanotherapy: Revisiting physical therapy and recruiting mechanobiology for a new era in medicine. *Trends Mol. Med.* **19**, 555–564 (2013).

15. J. G. McCarthy, E. J. Stelnicki, B. J. Mehrara, M. T. Longlaker, Distraction osteogenesis of the craniofacial skeleton. *Plast. Reconstr. Surg.* **107**, 1812–1827 (2001).

16. A. Bozkurt, A. Groger, D. O'Dey, F. Vogeler, A. Piatkowski, P. Ch. Fuchs, N. Pallua, Retrospective analysis of tissue expansion in reconstructive burn surgery: Evaluation of complication rates. *Burns* **34**, 1113–1118 (2008).

17. L. Lancerotto, D. P. Orgill, Mechanoregulation of angiogenesis in wound healing. *Adv. Wound Care* **3**, 626–634 (2014).

18. E. C. Novosel, C. Kleinhans, P. J. Kluger, Vascularization is the key challenge in tissue engineering. *Adv. Drug Deliv. Rev.* **63**, 300–311 (2011).

19. A. S. Mao, D. J. Mooney, Regenerative medicine: Current therapies and future directions. *Proc. Natl. Acad. Sci. U.S.A.* **112**, 14452–14459 (2015).

20. A. Atala, F. K. Kasper, A. G. Mikos, Engineering complex tissues. *Sci. Transl. Med.* **4**, 160rv12 (2012).

21. J. E. Foker, T. C. Kendall Krosch, K. Catton, F. Munro, K. M. Khan, Long-gap esophageal atresia treated by growth induction: The biological potential and early follow-up results. *Semin. Pediatr. Surg.* **18**, 23–29 (2009).

22. H. Koga, X. Sun, H. Yang, K. Nose, S. Somara, K. N. Bitar, C. Owyang, M. Okawada, D. H. Teitelbaum, Distraction-induced intestinal enterogenesis: Preservation of intestinal function and lengthening after reimplantation into normal jejunum. *Ann. Surg.* **255**, 302–310 (2012).

23. H. B. Kim, K. Vakili, B. P. Modi, M. A. Ferguson, A. P. Guillot, K. M. Potanos, S. P. Prabhu, S. J. Fishman, A novel treatment for the midaortic syndrome. *N. Engl. J. Med.* **367**, 2361–2362 (2012).

24. D. D. Damian, S. Arabagi, A. Fabozzo, P. Ngo, R. Jennings, M. Manfredi, P. E. Dupont, Robotic implant to apply tissue traction forces in the treatment of esophageal atresia, in *Proceedings of IEEE 2014 International Conference on Robotics and Automation (ICRA)* (IEEE, 2014), pp. 786–792.

25. P. F. M. Pinheiro, A. C. Simões e Silva, R. M. Pereira, Current knowledge on esophageal atresia. *World J. Gastroenterol.* **18**, 3662–3672 (2012).

26. M. H. Ross, G. I. Kaye, W. Pawlina, in *Histology: A Text and Atlas with Cell and Molecular Biology* (Lippincott Williams & Wilkins, ed. 4, 2002), pp. 479–481.

27. C. A. Powell, B. L. Smiley, J. Mills, H. H. Vandenburgh, Mechanical stimulation improves tissue-engineered human skeletal muscle. *Am. J. Physiol. Cell Physiol.* **283**, 1557–1565 (2002).

28. B.-S. Kim, J. Nikolovski, J. Bonadio, D. J. Mooney, Cyclic mechanical strain regulates the development of engineered smooth muscle tissue. *Nat. Biotechnol.* **17**, 979–983 (1999).

29. R. L. Mauck, M. A. Soltz, C. C. B. Wang, D. D. Wong, P.-H. G. Chao, W. B. Valhmu, C. T. Hung, G. A. Ateshian, Functional tissue engineering of articular cartilage through dynamic loading of chondrocyte- seeded agarose gels. *J. Biomech. Eng.* **122**, 252–260 (2000).

30. L. E. Niklason, J. Gao, W. M. Abbott, K. K. Hirschi, S. Houser, R. Marini, R. Langer, Functional arteries grown in vitro. *Science* **284**, 489–493 (1999).

31. L. Xu, S. R. Gutbrod, A. P. Bonifas, Y. Su, M. S. Sulkin, N. Lu, H.-J. Chung, K.-I. Jang, Z. Liu, M. Ying, C. Lu, R. C. Webb, J.-S. Kim, J. I. Laughner, H. Cheng, Y. Liu, A. Ameen, J.-W. Jeong, G.-T. Kim, Y. Huang, I. R. Efimov, J. A. Rogers, 3D multifunctional integumentary membranes for spatiotemporal cardiac measurements and stimulation across the entire epicardium. *Nat. Commun.* **5**, 3329 (2014).

32. G. Z. Lum, Z. Ye, X. Dong, H. Marvi, O. Erin, W. Hu, M. Sitti, Shape-programmable magnetic soft matter. *Proc. Natl. Acad. Sci. U.S.A.* **113**, E6007–E6015 (2016).

33. S. H. Lee, Y. B. Lee, B. H. Kim, C. Lee, Y. M. Cho, S.-N. Kim, C. G. Park, Y.-C. Cho, Y. B. Choy, Implantable batteryless device for on-demand and pulsatile insulin administration. *Nat. Commun.* **8**, 15032 (2017).

34. J. Kim, G. A. Salvatore, H. Araki, A. M. Chiarelli, Z. Xie, A. Banks, X. Sheng, Y. Liu, J. W. Lee, K.-I. Jang, S. Y. Heo, K. Cho, H. Luo, B. Zimmerman, J. Kim, L. Yan, X. Feng, S. Xu, M. Fabiani, G. Gratton, Y. Huang, U. Paik, J. A. Rogers, Battery-free, stretchable optoelectronic systems for wireless optical characterization of the skin. *Sci. Adv.* **2**, e1600418 (2016).

35. B. Lu, Y. Chen, D. Ou, H. Chen, L. Diao, W. Zhang, J. Zheng, W. Ma, L. Sun, X. Feng, Ultra-flexible piezoelectric devices integrated with heart to harvest the biomechanical energy. *Sci. Rep.* **5**, 16065 (2015).

Science Robotics

In vivo tissue regeneration with robotic implants

Dana D. DamianKarl PriceSlava ArabagiIgnacio BerraZurab MachaidzeSunil ManjilaShogo ShimadaAssunta FabozzoGustavo ArnalDavid Van StoryJeffrey D. GoldsmithAgoston T. AgostonChunwoo KimRussell W. JenningsPeter D. NgoMichael ManfrediPierre E. Dupont

View the article online
https://www.science.org/doi/10.1126/scirobotics.aaq0018
Permissions
https://www.science.org/help/reprints-and-permissions

Use of this article is subject to the Terms of service